AIAA JOURNAL
Vol. 30, No. 5, May 1992

High Alpha Aerodynamic Control by Tangential Fuselage Blowing

G. I. Font* and D. A. Tavella†
Stanford University, Stanford, California 94305

This work explores the effect of tangential blowing on the vortical structures that develop around a tangent-ogive cylinder configuration at high angle of attack. A lateral force results if blowing is applied asymmetrically. The study is conducted numerically by solving the three-dimensional, compressible-flow Navier-Stokes equations. The tangent cylinder is a simple configuration, therefore lowering the numerical cost and allowing for a more detailed investigation of the phenomena. The use of a tangent-ogive cylinder also facilitates the isolation of the important physical parameters. The computation was done for a Reynolds number of 52×10^4, Mach number of 0.2, blowing momentum coefficients of 0.0, 0.1, 0.2, and 0.4, and angles of attack of 10, 30, and 45 deg. Only asymmetrical blowing was considered. Surface streamlines, helicity contours, pressure distributions, and forces are obtained for each case.

Nomenclature

C_p	= pressure coefficient, $(p-p_\infty)/q_\infty$
C_y	= side force coefficient, force/$q_\infty S_{\text{ref}}$
C_μ	= blowing momentum coefficient
$\hat{F},\hat{G},\hat{H}$	= flux vectors
H	= helicity
J	= Jacobian of the coordinate transformation
M_∞	= Mach number
P	= pressure
$\hat{Q}$	= state vector
q_∞	= freestream dynamic pressure
R	= cylinder radius
Re_D	= Reynolds number based on diameter
S_j	= slot area
S_{ref}	= reference area
U	= flow velocity vector
u_j	= jet velocity vector
w	= vorticity vector
α	= angle of attack, deg
δ_j	= slot height
ξ,η,ζ	= body-fitted coordinates
ρ	= density

Subscripts

a	= aerodynamic component
c	= centrifugal component
D	= diameter
j	= jet
∞	= freestream reference conditions

Introduction

HIGHLY maneuverable aircraft or missiles operate at high angles of incidence where conventional control surfaces may fail to provide the required yaw control power. The craft may become directionally unstable and depart controlled flight. This problem has led to the intensive research into the origin and control of asymmetric side forces on slender forebodies. References 1-5 are several examples of this research effort. These studies explore the application of a jet on the nose region of a body to alter the flowfield and generate side forces.

The present work utilizes a long thin jet injected tangential to the surface from a slot longitudinally located on the body. The concept under study is shown in Fig. 1. A missile configuration is illustrated, but the control method is also applicable to aircraft with long forebodies. Tangential blowing supplies yaw control power by inducing controlled asymmetries in the flowfield about the missile forebody. Preliminary studies of this concept indicated that moderate blowing can generate yawing moments comparable with those produced by full rudder deflection at much lower angles of attack.[5]

This study explores in detail the flow structures and forces brought about by blowing. Reference 5 concentrated on verifying the approach and the numerical procedure on an F-18 forebody configuration. In the present study, the geometry was simplified to an ogive cylinder. This has the effect of reducing the numerical cost and allows for a larger matrix of blowing cases and angles of attack to be explored. The simplified geometry also allowed for the investigation and isolation of the different fundamental physical features from the effects of a complicated geometry.

Theoretical Background

Governing Equations

To facilitate the numerical solution, the equations for the conservation of mass, momentum, and energy may be written in the following form[6]:

$$\partial_\tau\hat{Q}+\partial_\xi(\hat{F}+\hat{F}_v)+\partial_\eta(\hat{G}+\hat{G}_v)+\partial_\zeta(\hat{H}+\hat{H}_v)=0 \qquad (1)$$

where τ represents time. The independent variables ξ, η, and ζ map a curvilinear body-conforming grid into a uniform computational space. The quantity $\hat{Q}$ is the vector of dependent flow variables; $\hat{F}=\hat{F}(\hat{Q})$, $\hat{G}=\hat{G}(\hat{Q})$, and $\hat{H}=\hat{H}(\hat{Q})$ are the inviscid flux vectors, whereas the terms $\hat{F}_v$, $\hat{G}_v$, and $\hat{H}_v$ are fluxes containing the viscous derivatives. Limiting these equations to the thin-layer approximations gives[7,8]

$$\partial_\tau\hat{Q}+\partial_\xi\hat{F}+\partial_\eta\hat{G}+\partial_\zeta\hat{H}=Re^{-1}\partial_\zeta\hat{S} \qquad (2)$$

Presented as Paper 91-0620 at the AIAA 29th Aerospace Sciences Meeting, Reno, NV, Jan. 7-10, 1991; received Jan. 21, 1991; revision received July 26, 1991; accepted for publication July 26, 1991.

*Graduate Research Assistant, Department of Aeronautics and Astronautics. Member AIAA.

†Senior Research Associate, Department of Aeronautics and Astronautics. Member AIAA.

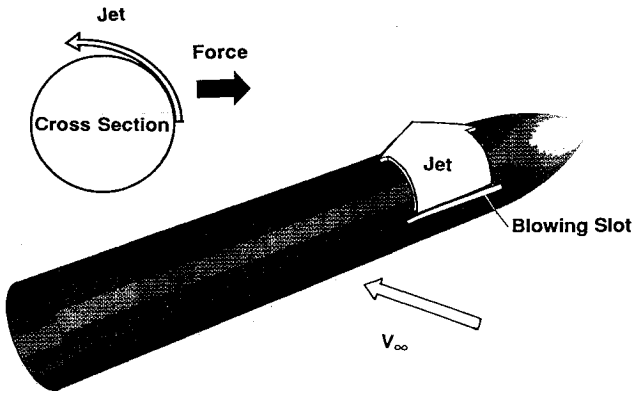

Fig. 1 Tangential blowing concept.

The only viscous terms retained are those in the ζ direction. These have been collected into the vector $\hat{S}$ and the nondimensional Reynolds number Re is factored from the viscous flux term.

To minimize numerical error, differencing is done about a known base solution. Denoting the base solution with subscript 0, Eq. (2) takes on the form

$$\delta_\tau(\hat{Q}-\hat{Q}_0)+\delta_\xi(\hat{F}-\hat{F}_0)+\delta_\eta(\hat{G}-\hat{G}_0)+\delta_\zeta(\hat{H}-\hat{H}_0)-Re^{-1}\delta_\zeta(\hat{S}-\hat{S}_0)=-\partial_\tau\hat{Q}_0-\partial_\xi\hat{F}_0-\partial_\eta\hat{G}_0-\partial_\zeta\hat{H}_0+Re^{-1}\partial_\zeta\hat{S}_0 \quad (3)$$

where δ indicates a general difference operator, and ∂ is the differential operator. The base state chosen for this work is the freestream. This forces the right-hand side of Eq. (3) to zero.

Numerical Algorithm

The solution of these equations is accomplished with the algorithm developed by Steger et al.[9] The algorithm uses flux-vector splitting[10] to upwind difference the convection terms in one coordinate direction (nominally streamwise). As discussed in Ref. 9, schemes using upwind differencing can have several advantages over methods that use central spatial differences in each direction. In particular, such schemes can have natural numerical dissipation and better stability properties. By using upwind differencing for the convective terms in the streamwise direction while retaining central differencing in the other directions, a two-factor implicit, approximately factored algorithm is obtained, which is unconditionally stable[11] for a representative model wave equation. The scheme may be written for the thin-layer Navier-Stokes equations in the form

$$[I+h\delta_\xi^b(\hat{A}^+)^n+h\delta_\zeta\hat{C}^n-hRe^{-1}\bar{\delta}_\zeta J^{-1}\hat{M}^nJ-D_i|_\zeta]\times[I+h\delta_\xi^f(\hat{A}^-)^n+h\delta_\eta\hat{B}^n-D_i|_\eta]\Delta\hat{Q}^n=\Delta t\{\delta_\xi^b[(\hat{F}^+)^n-\hat{F}_\infty^+]+\delta_\xi^f[(\hat{F}^-)^n-\hat{F}_\infty^-]+\delta_\eta(\hat{G}^n-\hat{G}_\infty)+\delta_\zeta(\hat{H}^n-\hat{H}_\infty)-Re^{-1}\bar{\delta}_\zeta(\hat{S}^n-\hat{S}_\infty)\}-D_e(\hat{Q}^n-\hat{Q}_\infty) \quad (4)$$

where $h=\Delta t$ or $\Delta t/2$ for first- or second-order time accuracy, and the freestream base solution is used, denoted by the subscript ∞. Second-order time accuracy is used when a nonsteady solution is required. In Eq. (4), δ is typically a three-point, second-order-accurate, central difference operator, $\bar{\delta}$ is a midpoint operator used with the viscous terms, and the operators δ_ξ^b and δ_ξ^f are backward and forward three-point difference operators. The flux $\hat{F}$ has been split into $\hat{F}^+$ and $\hat{F}^-$, according to the sign of the eigenvalues of the Jacobian matrix,[6] and the matrices $\hat{A}^\pm$, $\hat{B}$, $\hat{C}$, and $\hat{M}$ result from local linearization of the fluxes about $\hat{F}$, $\hat{G}$, $\hat{H}$, and $\hat{S}$, respectively. J denotes the Jacobian coordinate transformation. Dissipation operators D_e and D_i are used in the central space differencing directions. These are a combination of second- and fourth-order differences:

$$D_e|_\eta=(\Delta t)J^{-1}\left\{\epsilon_2\bar{\delta}|\hat{B}|\beta\bar{\delta}+\epsilon_4\bar{\delta}\frac{|\hat{B}|}{1+\beta}\bar{\delta}^3\right\}|_\eta J$$

$$D_i|_\eta=(\Delta t)J^{-1}\left\{\epsilon_2\bar{\delta}|\hat{B}|\beta\bar{\delta}+2.5\epsilon_4\bar{\delta}\frac{|\hat{B}|}{1+\beta}\bar{\delta}^3\right\}|_\eta J \quad (5)$$

where $\beta=|\bar{\delta}^2p|/|(1+\bar{\delta}^2)p|$ and $|\hat{B}|$ is the norm of the matrix $\hat{B}$ or an approximation. Here p is the nondimensional fluid pressure and ϵ_2 is $\mathcal{O}(1+M_\infty^2)$ whereas ϵ_4 is $\mathcal{O}(0.01)$. In this form, the second-order smoothing terms act to control numerical oscillations across shock waves, whereas the fourth-order smoothing is effective elsewhere. To improve the accuracy of the solutions, the fourth-order numerical smoothing terms are further scaled by the nondimensional local velocity ratio q/q_∞. This has the effect of reducing the numerical smoothing in the viscous layer adjoining the body surface where viscous dissipation controls the dispersion. In this region, large numerical smoothing terms can adversely affect the accuracy of the solution by modifying the physical viscous terms.

The Reynolds number in the present work is sufficiently low to insure laminar flow. Consequently, no turbulence was used. Preliminary studies of turbulence models for the jet are under way.

Computational Grid

The grid used in the computations around the tangent-ogive cylinder is shown in Fig. 2. It consists of $46\times100\times60$ points in the longitudinal, circumferential, and radial directions, respectively. The outer boundary is located 20 body diameters from the body surface, whereas the exit plane is located at the end of the body. Inflow boundary cells are set to freestream whereas the exit plane cells are explicitly updated through a zeroth-order extrapolation from the inner cells. These boundary conditions were found to give satisfactory results by Ref.

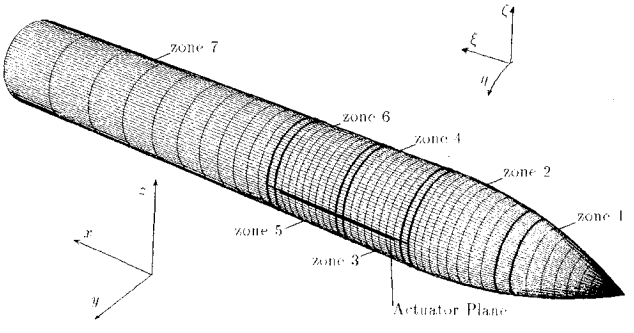

Fig. 2 Surface grid.

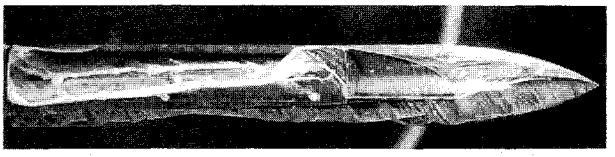

a) Oil flow visualization[13]: $Re_p=5.8\times10^4$; $M_\infty=0.06$

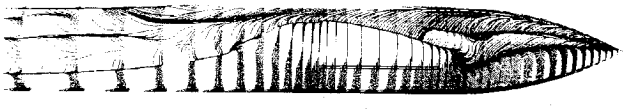

b) Simulated surface streamlines, $Re_p=5.2\times10^4$; $M_\infty=0.2$

Fig. 3 Surface streamline comparison: $\alpha=30$ deg; $C=0.0$.

12. The grid is divided into seven zones to allow computations in a 4MW queue on a Cray YMP. The solution on the zones that surround the entire body is accomplished through the use of a periodic solver option in F3D. Communication between the zones is done through one-cell overlapping. The flow variables on the boundary cells of one zone are explicitly set to the values of the corresponding point in the adjacent zone. The jet is implemented through the actuator plane concept.[5] In this approach, no attempt is made to model the fine details of the slot exit. However, the physics of the jet evolution and interaction are retained. Briefly, the jet flow variables are introduced explicitly as a discontinuity on a zonal boundary. The height and length of the discontinuity match the dimensions of the slot that is being modeled. The zonal boundaries are chosen to coincide with the location of the blowing slot. Consequently, zones 3–6 only extend over half of the circumference of the body and end at the location of the slot.

Results

Computed Cases

The tangent-ogive cylinder geometry is illustrated in Fig. 1. The configuration was chosen to match the experiments run by Celik and Roberts.[13] The model has a length of 11.55 in. and a diameter of 1.50 in. The ogive has a fineness ratio of 1.93. Only asymmetric blowing was considered for the production of side forces. Computations were carried out for $Re_D = 5.2 \times 10^4$, $M_\infty = 0.2$, $C_\mu = 0.0$, 0.1, 0.2, and 0.4, and $\alpha = 10$, 30, and 45 deg. All values, with the exception of the Mach number, were chosen to match the conditions of the experiment. The Mach number of the experiment was 0.06. The value used in the calculations was chosen to expedite convergence. The jet momentum coefficient is defined as

$$C_\mu = \frac{\rho_j V_j^2 S_j}{\frac{1}{2}\rho_\infty V_\infty^2 S_{\text{ref}}} \tag{6}$$

The reference area S_j is the body diameter multiplied by the slot length. The slot length was 1.333 diameters, the slot height 0.0147 diameters.

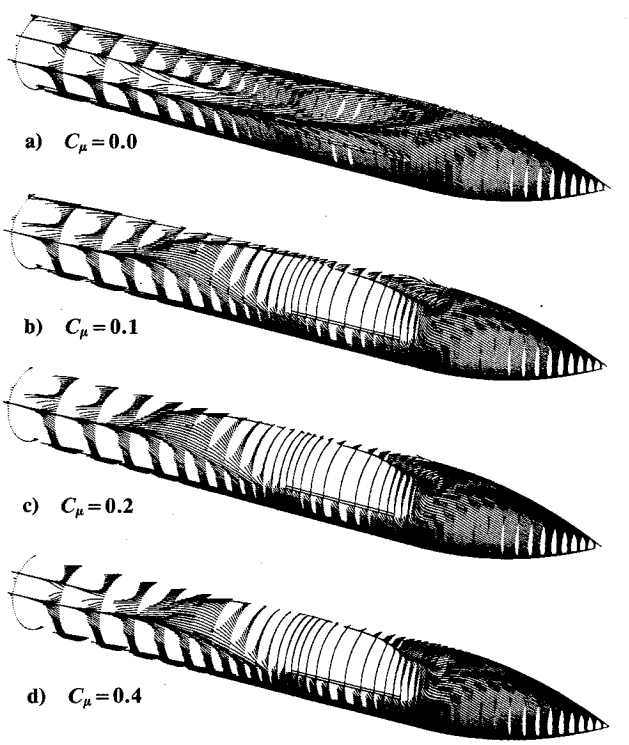

Fig. 4 Surface streamlines: $\alpha = 10$ deg; $Re_D = 5.2 \times 10^4$; $M_\infty = 0.2$.

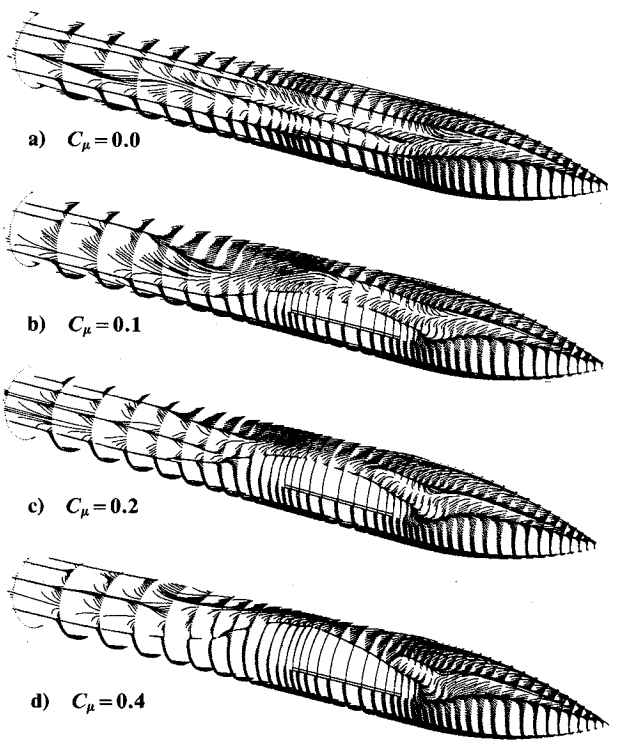

Fig. 5 Surface streamlines: $\alpha = 30$ deg; $Re_D = 5.2 \times 10^4$; $M_\infty = 0.2$.

Comparison with Experiment

The adequacy of boundary conditions and grid density were validated by comparison with the experiments done by Celik and Roberts.[13] Figure 3 shows the oil flow from the experiment and the surface streamlines from the computations for a blowing case. The blowing coefficient C_μ in these cases is 0.4. The oil flow shown in Fig. 3a indicates the flow pattern before the slot is not greatly affected. The primary separation line impinges on the beginning of the slot where the jet separation line starts. The jet remains attached until reaching the top of the body. The primary separation reforms at the end of the slot and moves toward the leeside of the body. Downstream of the slot, it joins with the jet separation line and moves back toward the windward side. Near the end of the body, it reaches a circumferential position slightly below the slot. A secondary separation line forms in the rear of the body. Figure 3b shows the simulated surface streamlines for the laminar computation. As in the experiment, the region forward of the slot is not affected greatly. The primary separation line, however, does not impinge on the beginning of the slot, as in the experiment. This is probably due to the absence of a geometrical definition of the slot in the computational grid. This may also be the reason that the computations fail to capture the reformation of the primary separation at the end of the slot. The jet in the laminar calculation does not reach the top of the body. Like the experiment, however, downstream of the slot, the jet separation line moves back toward the windward side, eventually reaching a circumferential position slightly below the slot. A secondary separation line is captured in the rear of the body, although it is located more leeward than observed in the experiment. A more detailed comparison with the experiment is presented in Ref. 14.

Surface Streamlines

Figure 4 shows the surface streamlines for the $\alpha = 10$ deg cases. Figure 4a shows the no-blowing case; the location of the slot is indicated for reference. The primary separation on the nose of the body is not well defined. Near the end of the body, it becomes sharper and a secondary separation also forms.

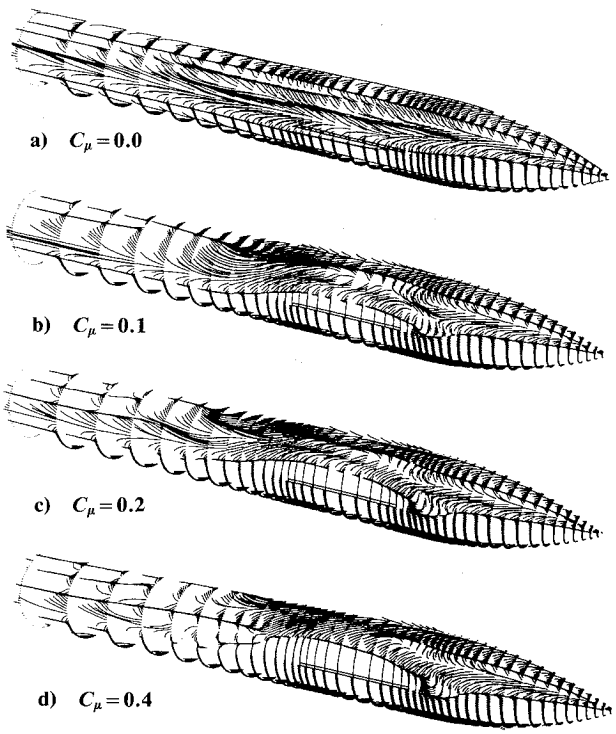

Fig. 6 Surface streamlines: $\alpha = 45$ deg; $RE_D = 5.2 \times 10^4$; $M_\infty = 0.2$.

Figure 4b shows the $C_\mu = 0.1$ case. The jet separates near the top of the body. The jet separation line continues upstream and downstream of the slot location. The downstream portion of the jet separation line ends before a primary separation line begins to take shape on the lower side of the body, near the slot. Figure 4c shows the $C_\mu = 0.2$ case. The general features are similar to the $C_\mu = 0.1$ case. There is no indication of a secondary separation. Figure 4d shows the $C_\mu = 0.4$ case. The jet separation, in this case, reaches the plane of symmetry. The primary separation begins to form from the end of the slot and becomes sharp near the end of the body. A secondary separation forms in the rear of the body.

Figure 5 shows the surface streamlines for $\alpha = 30$ deg. Figure 5a shows the no-blowing case. The primary and secondary separations form over the entire length of the body. The tertiary separation begins to form downstream of the cylinder-ogive nose junction. This separation disappears at a third of a body length downstream where another separation, closer azimuthally to the secondary separation, begins to form. Near the end of the body, a fourth separation is observed. Figure 5b shows the surface streamlines for the $C_\mu = 0.1$ case. The primary and secondary separation lines form on the nose. The jet separates after traveling a third of the distance up the side of the body. The jet separation line joins the primary separation upstream of the slot. Downstream of the slot, the jet separation does not remain on the upper part of the body as in the $\alpha = 10$ deg case. Instead, the jet separation moves downward and blends with the primary separation in the rear part of the body. The secondary separation reforms in the rear of the body. A tertiary separation also forms in the rear of the body. It lies azimuthally closer to the secondary separation. Figure 5c shows the surface streamlines for the $C_\mu = 0.2$ case. The jet travels farther than in the $C_\mu = 0.1$ case before separating. The secondary separation line ends closer to the forward part of the slot region. A separation line, in the same azimuthal location, is observed to start in the region where the jet separation blends with the primary separation. In the rear of the body, a third separation line forms near the top of the body but below the secondary separation line. Figure 5d shows the surface streamlines for the $C_\mu = 0.4$ case. The secondary separation line is not as sharp as in the $C_\mu = 0.2$ case. The maximum excursion of jet separation line is located three-quarters of the way up the side of the body. Farther downstream, the jet separation line moves down to blend with the primary separation. Secondary and tertiary separation lines are captured in the rear of the body. A fourth separation line is also captured near the end of the body.

Figure 6 shows the surface streamlines for $\alpha = 45$ deg. Figure 6a shows the no-blowing case. The primary and secondary separation lines form over the entire body. A tertiary separation forms near the midpoint of the body. This separation line disappears and reforms before the body ends. Figure 6b shows the $C_\mu = 0.1$ case. The primary separation line starts at the nose and joins the separation line that is located a quarter of the way up the side of the body. The secondary separation line

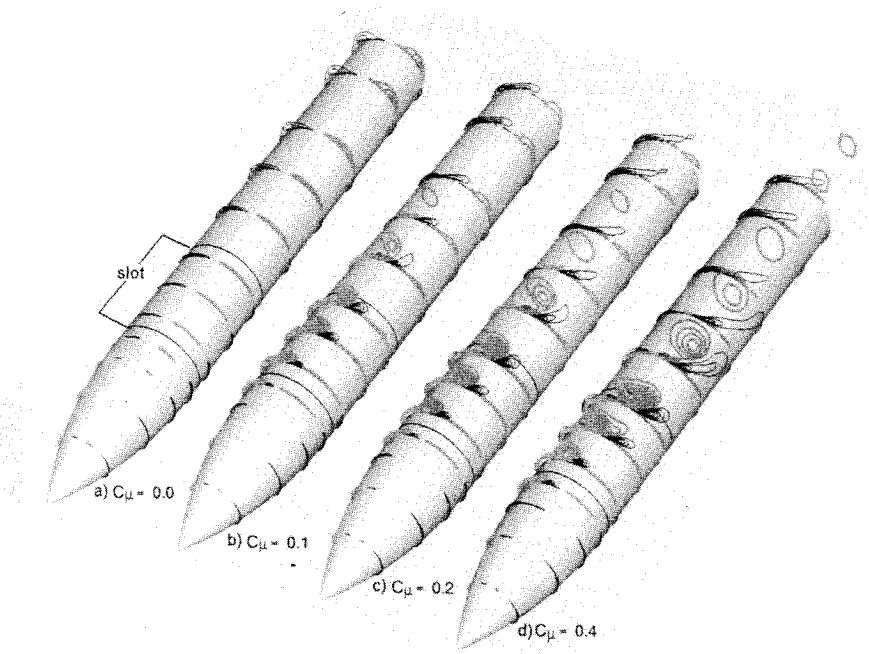

Fig. 7 Helicity contours: $\alpha = 10$ deg; $Re_D = 5.2 \times 10^4$; $M_\infty = 0.2$.

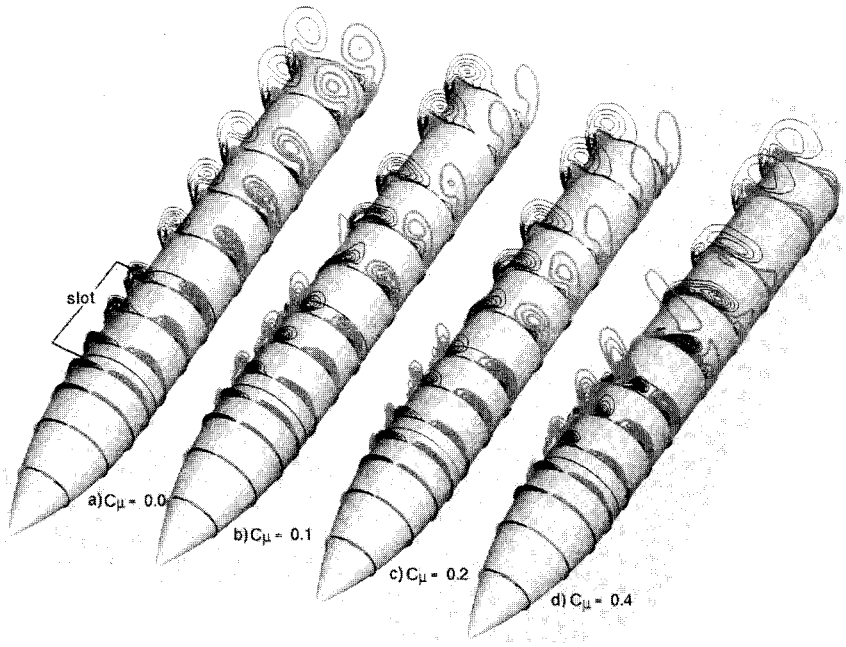

Fig. 8 Helicity contours: $\alpha = 13$ deg; $Re_D = 5.2 \times 10^4$; $M_\infty = 0.2$.

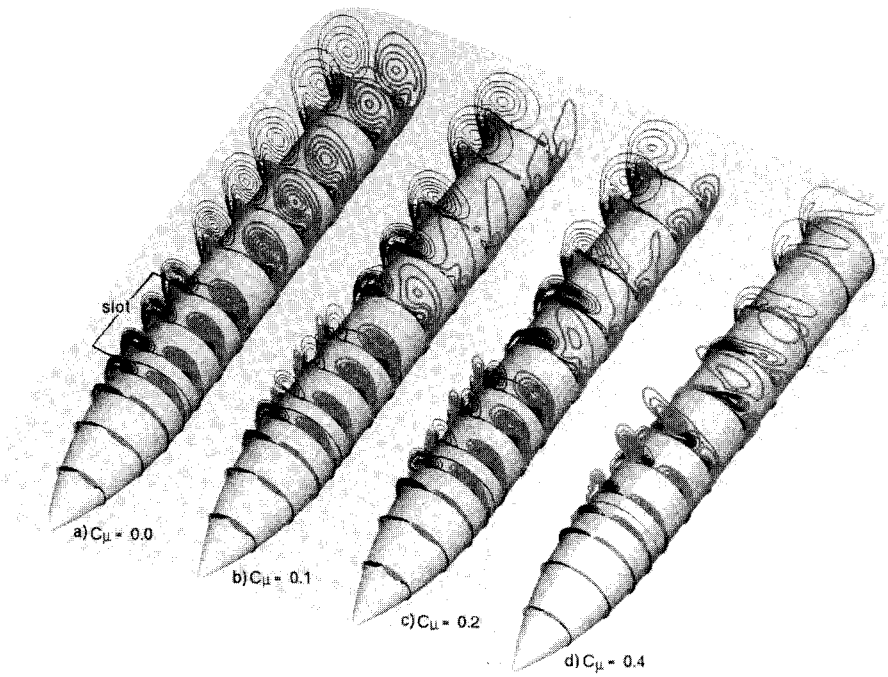

Fig. 9 Helicity contours: $\alpha = 45$ deg; $Re_D = 5.2 \times 10^4$; $M_\infty = 0.2$.

also starts at the nose and is well defined until a short distance downstream of the end of the slot. The jet separation line smoothly blends with the primary separation line after the slot ends. Secondary and tertiary separation lines are captured in the rear of the body. Figure 6c shows the surface streamlines for the $C_\mu = 0.2$ case. The features are similar to the $C_\mu = 0.1$ case, although the jet remains attached longer and a fourth separation line is observed in the rear body. Figure 6d shows the $C_\mu = 0.4$ case. Downstream of the slot, the primary separation line is not well defined. The secondary separation line begins almost at the maximum excursion point of the jet separation line and proceeds to the end of the body. A tertiary separation line is captured near the end of the body.

Helicity Density Contours

Helicity density contours are used to visualize the vortical structure of the flowfield. Helicity density is defined as[15] $H = U \cdot w$. If the main component of velocity and vorticity vectors are perpendicular to the plane used to define the contours, then the color of the helicity contour is indicative of the sense of rotation of the fluid. This condition is met above the upper surface of the body, outside the boundary layers. At each station, the outermost contour line has a value of 0.05. The increment between contour lines is also 0.05. For brevity, helicity density will be referred to as helicity in the remainder of this section.

Figure 7 shows the helicity contours for the $\alpha = 10$ deg cases. The viewpoint is from the top and the side opposite the slot. The slot is located on the far side of each body, between the two circumferential lines, as indicated in the figures. This viewpoint was chosen as the one best displaying the helicity contour details on both sides of the body. Figure 7a shows the

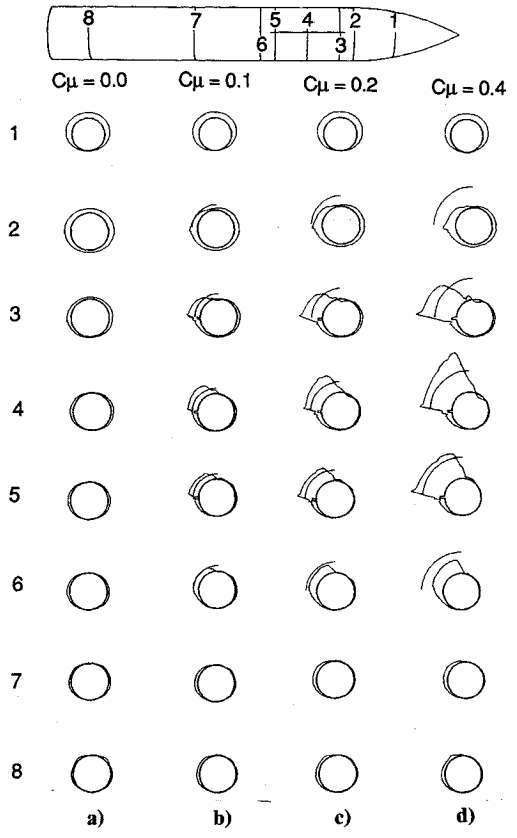

Fig. 10 Cross-sectional pressure distribution: $\alpha = 10$ deg; $Re_D = 5.2 \times 10^4$; $M_\infty = 0.2$.

helicity contours for the no-blowing case. The flow above the upper surface of the body is not massively separated, as indicated by the size of the helicity contours. The black-colored contours on the slot side indicate a clockwise sense of rotation, when viewed aft from the nose. The gray-colored contours indicate flow rotation in the opposite sense. Figure 7b shows the helicity contours for $C_\mu = 0.1$. Large helicity contours of both black and gray coloration are observed over the region of the slot. These contours start from the slot side and extend over the upper surface of the body. They indicate that the flow is rotating in both directions on the side of the slot. The helicity contours on the side of the body opposite the slot are not noticeably altegray by the presence of the jet. Downstream, the black helicity contours remain near the surface. By the end of the body, the helicity contours resemble the no-blowing case, although the contours on the slot side are larger and more elongated. Figure 7c shows the helicity contours for $C_\mu = 0.2$. The pattern in the slot region qualitatively resembles the $C_\mu = 0.1$ case, although the features are larger. The flowfield near the end of the body no longer resembles that of the no-blowing case. The black helicity contour on the slot side is larger and more elongated whereas the gray contour on the opposite side is very small. Figure 7d shows the helicity contours for $C_\mu = 0.4$. In the slot region on the slot side, black and gray helicity contours are observed with the gray contours larger than the black ones. On the opposite side of the body, the helicity contours do not differ from the no-blowing case. Downstream of the slot region, the pattern is similar to the $C_\mu = 0.2$ case. By the end of the body, the black helicity contours are no longer found over the upper top of the body; instead, they are found on the slot side. On the opposite side, gray helicity contours are almost nonexistent.

Figure 8 shows the helicity contours for the cases with $\alpha = 30$ deg. Figure 8a shows the no-blowing case. The flow at this angle of attack is significantly more separated as indicated by the size of the helicity contours. The primary vortex is located at the center of the helicity contour. It gradually moves away from the surface as it proceeds toward the rear of the body. The secondary vortex is identified on the figure with the small region of contrasting color close to the surface and below (or inboard) of the main contour, as indicated by the small gray region under the black lobes on the slot side. These regions grow in size near the end of the body. Figure 8b shows the $C_\mu = 0.1$ case. In the region of the slot, on the side of the body, the helicity contours are both black and gray, indicating flow rotation in both directions. Opposite the slot, the helicity contours retain the same shape and color as in the no-blowing case. Downstream of the slot region, on the slot side, the black helicity contours are larger and lie closer to the surface than in the no-blowing case. Figure 8c shows the $C_\mu = 0.2$ case. The pattern in the slot region, except for larger contours on the slot side, mirror the $C_\mu = 0.1$ case, with the exception that the gray helicity contours on the slot side are still observed further downstream. The black helicity contours, although increasing in size, remain in contact with the surface through the end of the body. The gray helicity contours on the opposite side diminish in size as the flow moves downstream. Figure 8d shows the $C_\mu = 0.4$ case. In the slot region on the slot side, the gray helicity contours are larger and more elongated away from the body than in the $C_\mu = 0.2$ case. On the side opposite the slot, the helicity structures resemble their no-blowing counterparts in size and color. Immediately downstream of the slot, the black helicity contour from the jet side is observed over the upper surface of the body whereas the gray contour has stretched away from the surface. On the opposite side, the gray helicity structure is already diminished in size. It ends where the black helicity from the jet side begins. Farther down the body, a small lobe at a large distance from the surface is the only sign of the counter-clockwise rotating flow. This lobe appears, in the figure, underneath the third helicity contour,

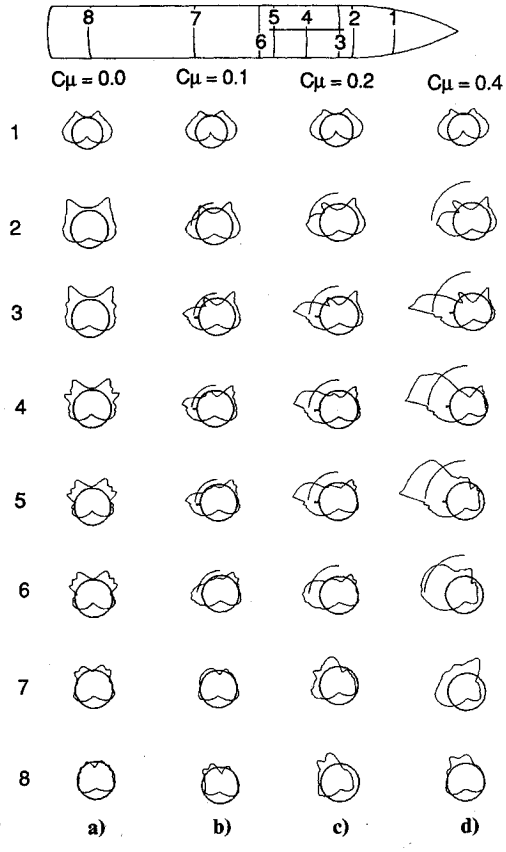

Fig. 11 Cross-sectional pressure distribution: $\alpha = 30$ deg; $Re_D = 5.2 \times 10^4$; $M_\infty = 0.2$.

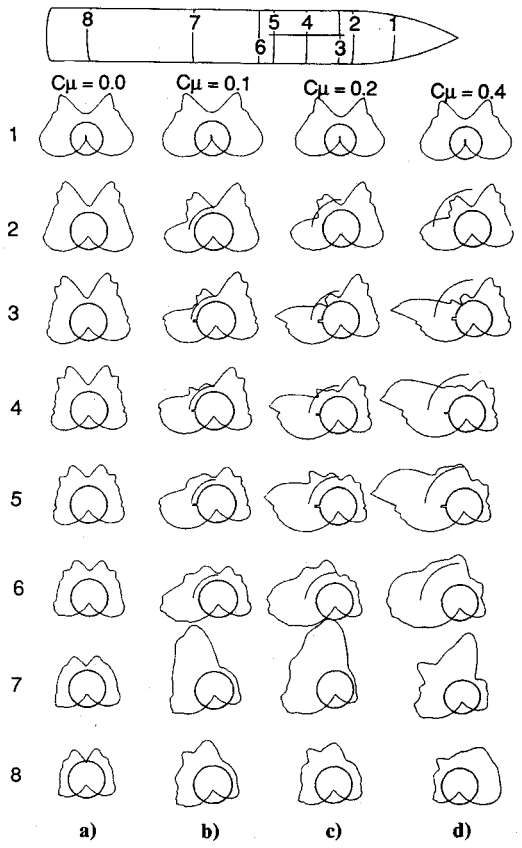

Fig. 12 Cross-sectional pressure distribution: $\alpha = 45$ deg; $Re_D = 5.2 \times 10^4$; $M_\infty = 0.2$.

counting from the rear of the body, on the slot side. The black helicity structure at this station is large in comparison with both the $C_\mu = 0.2$ and the no-blowing case and is located very close to the surface. At this station, on the side opposite the slot, the gray helicity contours are very small. Downstream of this station, the helicity contours on the slot side begin to look like the contours in the no-blowing case. Those on the opposite side, although beginning to grow, do not attain their no-blowing size or shape.

Figure 9 shows the helicity contours for the cases with $\alpha = 45$ deg. Figure 9a displays the no-blowing case. The helicity contours are very large, indicating the presence of greatly separated regions. These regions form the primary vortex system. The secondary vortex is also captured and increases in size as it proceeds to the rear of the body. Figure 9b shows the $C_\mu = 0.1$ case. In the region of the slot on the slot side, the helicity contours indicate the presence of flow rotation in both directions. On the opposite side, the helicity contours are unaltered by the presence of the jet. Downstream of the slot region, on the slot side, no gray helicity contour is observed. The black helicity contour is smaller than in the no-blowing case, but is more dense, and is located closer to the surface. On the opposite side, the gray helicity contours are less dense, as indicated by fewer contour lines, than in the no-blowing case. Downstream of this region, the contours on the slot side continue to increase in size, although they remain near the surface. The contours on the opposite side diminish in size and their shape becomes more elongated. Figure 9c shows the $C_\mu = 0.2$ case. The contours in the slot region are similar to the $C_\mu = 0.1$ case. Downstream of this region a small lobe of the gray helicity is observed on the slot side of the body. Opposite this, the gray helicity contour is more elongated but also smaller than in the previous case. In the rear of the body, the slot side helicity contours are comparable with the no-blowing case. The contours on the opposite side have a greatly diminished size. Figure 9d shows the $C_\mu = 0.4$ case. The contours in the slot region on the slot side are larger but otherwise similar in shape and color to the previous case. The helicity contours on the opposite side do not remain unaltered in this case but diminish in size. Downstream of the slot region on the slot side, the black helicity contours have an intensity greater than in the no-blowing case. A large gray helicity contour is observed on the slot side at a greater distance from the surface than the aforementioned black contours. At the same station on the opposite side, the gray helicity contour is less intense (it has fewer contour lines) than the no-blowing case but is larger and more elongated. Downstream of this station, on the blowing side, the black helicity contour is large and close to the upper surface of the body. The gray helicity contour on the opposite side is split in two parts, one above the other. Near the end of the body, the slot-side helicity contours resemble their no-blowing shape. On the opposite side, the helicity contours are small and remain close to the body.

Pressure Distributions

Figures 10–12 show the pressure contours plotted in polar form at selected streamwise stations along the body. This was done to facilitate comparison between pressure characteristics and flow features identified by the streamline and helicity contours. A negative pressure value lies outside the circle whereas a positive value lies inside. All contours are plotted in the same scale. The slot location is indicated on the figures with a small dash perpendicular to the circle. Only those stations along the slot contain the dash. The concentric arc indicates the centrifugal component of C_p. This will be explained later in the discussion section. For comparison, this

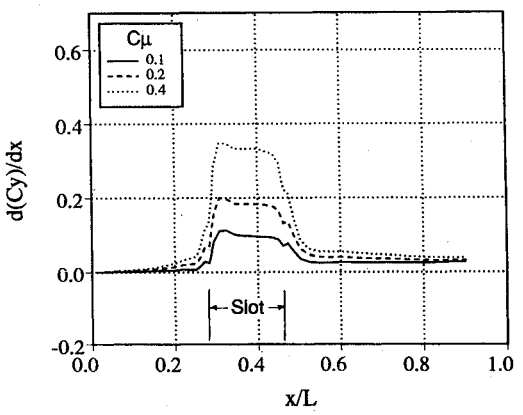

Fig. 13 Side force distribution: $\alpha = 10$ deg; $Re_D = 5.2 \times 10^4$; $M_\infty = 0.2$.

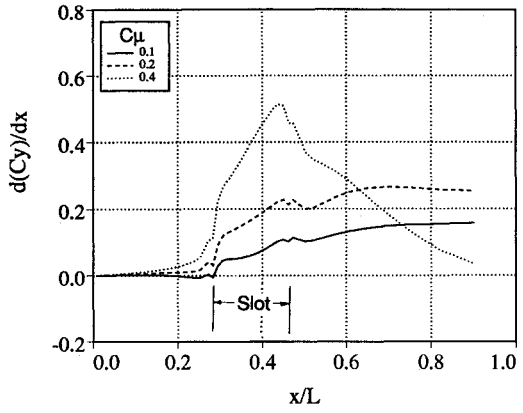

Fig. 14 Side force distribution: $\alpha = 30$ deg; $Re_D = 5.2 \times 10^4$; $M_\infty = 0.2$.

arc is plotted, for the blowing cases, at stations immediately before the start of the slot, those along the slot, and those immediately after the end of the slot.

Figure 10 shows the pressure contours for $\alpha = 10$ deg at C_μ equal to 0.0, 0.1, 0.2, and 0.4. Figure 10a displays the no-blowing case. The pressure contours are uniformly symmetrical about the vertical axis. The pressure reaches its lowest value near where the ogive nose joins with the cylinder. The lack of bumps in the pressure contours near the upper surface of the body are indicative of a flowfield that is almost completely attached. Figure 10b shows the pressure contours at $C_\mu = 0.1$. The pressure begins to drop on the slot side at station 2, before the beginning of the slot. In the slot region, a low-pressure zone is observed below the slot. A discontinuity in the pressure contour is present at the slot. This discontinuity does not exist for stations not containing the slot. Comparison with the streamlines in Figs. 3-5 reveals that the azimuthal point where $C_p = 0$ is very close to the separation point of the jet. The stations near the rear of the body retain the low-pressure zone on the side of the slot, although its magnitude is greatly diminished. The low-pressure regions occur at the locations where the blue helicity contours were observed in the aftbody. Figures 10c and 10d show the pressure contours for $C_\mu = 0.2$ and 0.4, respectively. The characteristics are similar to the $C_\mu = 0.1$ case, although the magnitudes are greater and the discontinuity at the slot is more pronounced.

Figure 11 shows the pressure contours for $\alpha = 30$ deg at $C_\mu = 0.0$, 0.1, 0.2, and 0.4. Figure 11a displays the no-blowing case. The pressure minima begin at a lower value than in the $\alpha = 10$ deg case and increase toward the end of the body where positive pressure is felt over most of the surface. The component of velocity that stagnates at the lower part of the body is

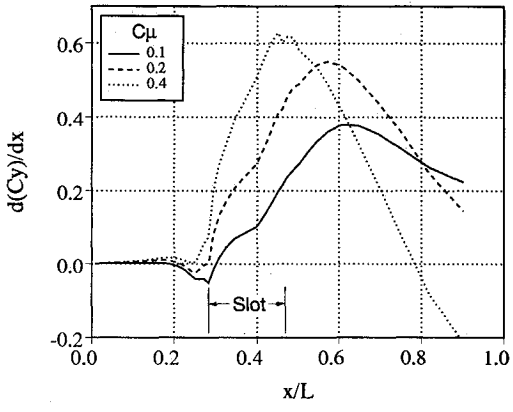

Fig. 15 Side force distribution: $\alpha = 45$ deg; $Re_D = 5.2 \times 10^4$; $M_\infty = 0.2$.

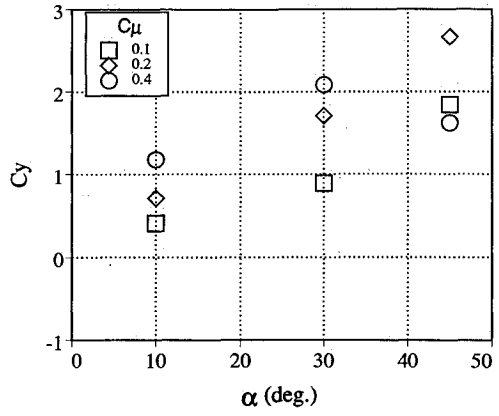

Fig. 16 Side force: $Re_D = 5.2 \times 10^4$; $M_\infty = 0.2$.

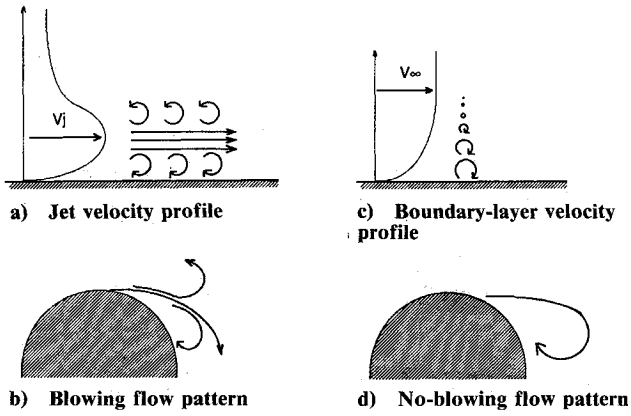

Fig. 17 Conceptual model.

indicated by a positive pressure peak on the lower side of the plots. Figure 11b shows the $C_\mu = 0.1$ case. A low-pressure bulge of the contours is observed along the slot. The larger portion of this bulge is located on the lower side of the body, azimuthally before the slot. The pressure contours opposite the slot generally retain their no-blowing shape and magnitude in the forward part of the slot. In the rear part, the pressure begins to increase. Downstream of the slot region, the pressure continues to increase until, by the end of the body, only the upper quadrant on the slot side has suction. Figure 11c shows the $C_\mu = 0.2$ case. The discontinuity first observed in the $\alpha = 10$ deg cases is now easily discernible. The details along the slot resemble those of the $C_\mu = 0.1$ case, although the magnitudes are greater. In the region of the body downstream of the slot, however, the low-pressure region is maintained to the end of the body. Figure 11d shows the $C_\mu = 0.4$ case. The pattern along the slot on the slot side is similar to the $C_\mu = 0.2$ case. On the side opposite the slot, however, the pressure becomes significantly greater before the end of the slot. Downstream of the slot, the low-pressure region exists, not only on the slot side, but also on the upper surface of the body, where a large blue helicity contour was observed close to the surface. Toward the end of the body, the low pressure is confined to the upper surface and is diminished in magnitude.

Figure 12 shows the polar pressure plots for $\alpha = 45$ deg for $C_\mu = 0.0$, 0.1, 0.2, and 0.4. Figure 12a displays the no-blowing case. The contours are symmetrical about the vertical axis of the body. The magnitudes of the low-pressure regions are greater in the forward sections of the body than in the aft sections. Figure 12b shows the $C_\mu = 0.1$ case. The disturbance introduced by the jet on the slot side can be observed before the beginning of the slot. The pressure on the side opposite the slot is unaltered. The low-pressure region along the slot is, to a large extent, on the lower quadrant of the body. Over the upper, slot-side quadrant, the pressure is actually greater than in the no-blowing case. Oppsite the slot, the pressure contours are unaltered. Downstream of the slot, the pressure in the upper, slot-side quadrant becomes more negative. On the opposite side, the pressure is observed to increase, when compared with the no-blowing case. At station 7, a region of negative pressure more intense than that along the slot forms on the slot side and along the upper surface of the body. This peak diminishes in magnitude toward the end of the body. Figure 12c shows the $C_\mu = 0.2$ case. A discontinuity in the pressure contours is observed at the slot. The low-pressure region along the slot extends over a greater portion of the upper, slot-side quadrant than in the $C_\mu = 0.1$ case. This corresponds to the jet remaining attached longer along the body. Details downstream of the slot follow the same pattern as the $C_\mu = 0.1$ case, although the magnitudes are greater. Figure 12d shows the $C_\mu = 0.4$ case. The discontinuity in the pressure

contours at the slot is more prominent in this case. The low-pressure region over the upper surface of the body occurs before the slot ends. Downstream of the slot, the pressure on the slot side increases, whereas that on the side opposite the slot decreases. The end of the body displays lower pressure on the side opposite the slot.

Force Computations

Figures 13–15 show the distributions of side force coefficient per unit length along the body (c_y vs x). The slot extends from $x/L = 0.28$ to 0.46, as indicated on the figures. Figure 13 shows the $\alpha = 10$ deg cases. For the three blowing ratios, the side force increases rapidly where the slot begins and remains fairly constant along the slot. Where the slot ends, the force for the three cases decreases rapidly, although it does not return to zero. In the rear of the body, a small lateral force remains for all values of C_μ. Figure 14 shows the $\alpha = 30$ deg cases. The force for the three blowing ratios first rises to an initial value at the start of the slot and subsequently increases along the length of the slot. The force in the aftbody, for the $C_\mu = 0.1$ and 0.2 cases, does not remain constant, as in the $\alpha = 10$ deg cases, but continues to increase. For the case of $C_\mu = 0.4$, the force decreases along the entire aftbody. Figure 15 shows the $\alpha = 45$ deg cases. The side force for the lower values of C_μ (0.1 and 0.2) increase throughout the slot region and continue to increase after the point where the slot ends. After a maximum is reached downstream of the slot, the force begins to decrease. The $C_\mu = 0.4$ case reaches its maximum at the end of the slot. It begins to decrease, and by the end of the body, it has become negative.

Figure 16 shows the lateral force coefficient vs angle of attack (C_y vs α). For low and moderate blowing ratios ($C_\mu =$ 0.1 and 0.2), the force increases with angle of attack. Also, the rate of increase of side force ($dC_y/d\alpha$) is larger at higher angles of attack. At high angles of attack, however, the rate of increase becomes negative. Specifically, for $\alpha = 45$ deg and $C_\mu = 0.4$, the side force produced by blowing is lower than that produced at $C_\mu = 0.1$. This is due to the force reversal identified near the end of the body in Figs. 12d and 15.

Discussion

The force produced by a jet moving along a curved wall has several components. The first arises from the centrifugal pressure gradient. The centrifugal force component may be estimated by carrying out a force balance on a differential fluid mass element that is traveling in circular motion with the velocity of the jet and at the radius of the wall. Normalizing by a differential area then gives an estimate for the pressure at the wall due to the jet centrifugal force:

$$P_c = \frac{\rho_j u_j^2 \delta_j}{R} \tag{7}$$

where δ_j is the jet thickness and R is the radius of the wall. Normalizing by the reference area and the freestream dynamic pressure gives the nondimensional pressure as

$$C_{p_c} = 2C_\mu \tag{8}$$

The quantity C_{p_c} is plotted in Figs. 10–12 as the concentric arc in the upper left quadrant of each station in the region of the slot. In each case, C_{p_c} closely matches the magnitude of the discontinuous jump in the pressure contour at the slot. The fact that the discontinuity is observed only in the region of the slot indicates that the jump is due to the presence of the jet. As the angle of attack increases, the contribution of the centrifugal component to the total force diminishes due to the early separation of the jet. The cross-sectional pressure distributions (Figs. 10–12) indicate that at $\alpha = 10$ deg the centrifugal force component is more than 50% of the side force in the slot region, whereas at $\alpha = 45$ deg it is less than 30%.

The second component of the force generated by the blowing is due to the aerodynamic interaction. This interaction results from a modification of the local characteristics of the flow over the surface that, in turn, modify the global characteristics of the flowfield around the body. Figure 17 compares the global and local flow features associated with the no-blowing and blowing cases. Comparison of the pressure plots (Figs. 10–12) with the helicity contour plots (Figs. 7–9) reveals that the regions of lowest pressure coincide with the regions of largest intensity of vorticity. It may be assumed that these regions arise from the vorticity created by the jet shear (Figs. 17a and 17b) and perhaps through interaction of the jet-furnished vorticity with the vorticity already present in the flow (Figs. 17c and 17d). This interaction is capable of generating side forces, not only along the slot, but downstream as well (Figs. 13–15). With blowing strength sufficiently high, the force may reverse downstream of the slot (Fig. 15, $C_\mu = 0.4$). This causes the total side force to decrease with increasing blowing strength. For example, $C_\mu = 0.4$, $\alpha = 45$ deg in Fig. 16.

Conclusions

A numerical study of the effects of tangential blowing on the flowfield around a tangent-ogive cylinder configuration has been conducted. The following observations are made:

1) Large side forces may be generated with modest blowing mass-flow requirements by employing a tangential jet.

2) Side forces are induced by the jet through at least two major mechanisms: the centrifugal force developed when the jet follows the curvature of the surface and the decrease in pressure associated with the vorticity supplied by the jet.

3) At moderate jet momentum coefficients, the side force generally increases with increasing angle of attack. At high jet momentum coefficients, however, the side force can decrease with increasing angle of attack.

4) At moderate angles of attack, the side force increases with increasing jet momentum coefficient. This trend can reverse at high angles of attack and high jet momentum coefficients.

5) At high jet momentum coefficients, the local side force vector may reverse direction at stations downstream of the slot.

6) At high angles of attack, the largest side forces may occur downstream of the slot.

Acknowledgments

This work was sponsored by NASA Ames Research Center under NASA Contract NCC 2-55. The authors wish to thank L. Roberts and L. Schiff for their logistical and technical support.

References

[1]Ng, T. T., and Malcolm, G. N., "Aerodynamic Control Using Forebody Blowing and Suction," AIAA Paper 91-0619, Jan. 1991.

[2]Degani, D., and Schiff, L. B., "Numeric Simulation of the Effect of Spatial Disturbances on Vortex Asymmetry," AIAA Paper 89-0340, Jan. 1989.

[3]Malcolm, G. N., Ng, T. T., and Lewis, L. C., "Development of Non-Conventional Control Methods for High Angle of Attack Flight Using Vortex Manipulation," AIAA Paper 89-2192, July 1989.

[4]Rosen, B. S., and Davis, W. H., "Numerical Study of Asymmetric Angle-of-Attack Forebody Vortices on the X-29 Aircraft," AIAA Paper 90-3004, Aug. 1990.

[5]Tavella, D. A., Schiff, L. B., and Cummings, R., "Pneumatic Vortical Flow Control at High Angles of Attack," AIAA Paper 90-0098, Jan. 1990.

[6]Viviand, H., "Conservative Forms of Gas Dynamics Equations," *La Recherche Aerospatiale,* Vol. 1, 1974, pp. 65–68.

[7]Steger, J. L., "Implicit Finite-Difference Simulation of Flow about Arbitrary Two-Dimensional Geometries," *AIAA Journal,* Vol. 16, 1978, pp. 679–686.

[8]Baldwin, B. S., and Lomax, H., "Thin Layer Approximation and Algebraic Model for Separated Turbulent Flows," AIAA Paper 78-257, Jan. 1978.

[9]Steger, J. L., Ying, S. X., and Schiff, L. B., "A Partially Flux-Split Algorithm for Numerical Simulation of Unsteady Viscous Flows," *Proceedings of a Workshop on Computational Fluid Dynamics,* Univ. of California, Davis, CA, 1986.

[10]Ying, S. X., "Three-Dimensional Implicit Approximately Factored Schemes for Equations in Gasdynamics," Ph.D. Thesis, Stanford Univ., Stanford, CA, 1986; also SUDAAR 557, June 1986.

[11]Flores, J., and Chaderjian, N. M., "The Numerical Simulation of Transonic Separated Flow about the Complete F-16A," AIAA Paper 88-2506, June 1988.

[12]Schiff, L. B., Degani, D., and Cummings, R. M., "Numerical Simulation of Separated and Vortical Flows on Bodies at Large Angles of Attack," Fourth Symposium on Numerical and Physical Aspects of Aerodynamic Flows, California State Univ., Long Beach, CA, Jan. 1989.

[13]Celik, Z. Z., and Roberts, L., "Experimental Results of the Control of Lateral Forces on a Slender Body," Joint Institute for Aeronautics and Acoustics, Stanford Univ., JIAA-TR-100, Stanford, CA, Jan. 1991.

[14]Font, G. I., Celik, Z. Z., and Roberts, L., "Numerical and Experimental Study of Tangential Jet Blowing Applied to Bodies at High Alpha," AIAA Paper 91-3253, Sept. 1991.

[15]Levy, Y., Seginer, A., and Degani, D., "Graphical Representation of Three-Dimensional Vortical Flows by Means of Helicity Density and Normalized Helicity," AIAA Paper 88-2598, June 1988.